20th International Congress of Chemical and Process Engineering CHISA 2012
25 – 29 August 2012, Prague, Czech Republic

# Gas/particle interaction in ultrasound agitated gas flow

Claas Knoop [a]*, Udo Fritsching

*Institiut für Werkstofftechnik, Badgasteiner Straße 3, D-28359 Bremen, Germany*

**Abstract**

Acoustic waves imply specific force and stress distributions onto particles in a gaseous environment. In this paper time-dependent and time-averaged acoustic forces of resonant standing ultrasound waves on rigid particles and agglomerates in gaseous environment are investigated by numerical simulation. The calculated resonant standing wave field is validated using experimental data. Acoustic forces are calculated for cylindrical and spherical particle geometries and the resulting values are compared with analytic correlations from literature. The position of the bodies in respect to the sound source was varied to study the local dependence of the acoustic force. Characteristics of gas/particle interaction in ultrasound agitated gas flow are discussed.

*Keywords:* Direct numerical solution; resonant ultrasound; acoustic radiation force

## 1. Introduction

Several technical applications deal with dispersions being exposed to acoustic fields. Examples are acoustic levitation [1], ultrasonic-standing-wave-atomization [2,3], ultrasonic separation [4] and standing wave manipulation of particles and cells [5]. Since it is necessary to know the forces on the dispersed phase in many cases, a number of publications on acoustic forces on particles have been published. One of the first was King who established theories to calculate the acoustic radiation force on rigid spheres [6]

---

* Corresponding author.
*E-mail address*: knoop@iwt.uni-bremen.de

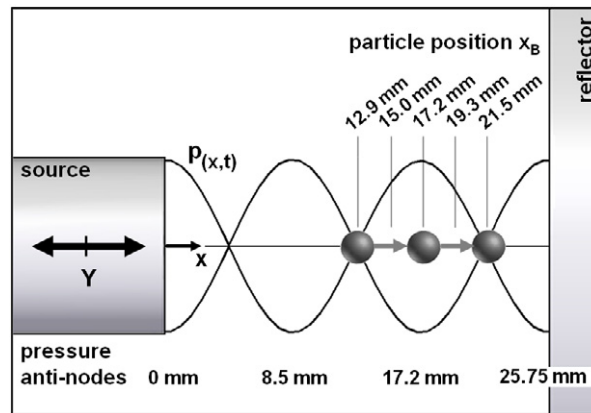and discs [7] for planar travelling as well as for standing waves. An approach to calculate the forces on



Fig. 1. Schematic sound wave setup

cylinders was presented by Awatani [8]. Based on Kings and Awatanis work, formulations were developed to consider compressible, elastic spheres/cylinders in sound fields [9-11]. While King was neglecting the viscosity of the fluid, Westervelt [12,13] considered viscid sound fields and the effects of the boundary layer. Based on that, Danilov and Mironov derived the mean force on small spherical particles where the effects of dissipation can not be neglected [14]. Here it may be distinguished between the total mean force and the radiation force. For inviscid fluids the two forces are identical. However, due to nonlinear effects such as acoustic streaming the forces may differ significantly. Another well-known approach for the determination of the acoustic radiation force was followed by Gor'kov [15]. He calculated the scattered wave potential based on the solution of a potential incompressible flow past a spherical particle.

In this contribution gas/particle interaction and the resulting forces will be calculated within numerical simulations for particles emerged in gaseous environment and stressed by high intensity acoustic field. In this way static and dynamic forces on the particle can be extracted

## 2. Theoretical approaches

The setup used for the numerical calculations is given in Figure 1. It is based on an experimental levitation system with a sound source alternating with an elongation $Y$ and a passive reflector. The distance between source and sensor is set in a way that a resonant standing wave field is created with a number of three pressure nodes along the x-axis. The particle position $x_B$ is varied between 12.9 mm and 21.5 mm.

In this work the time dependent pressure field $p_s$ on the surface of cylindrical and spherical particles caused by resonant standing ultrasound is calculated by means of a direct solution of the compressible Navier-Stokes equations (1, 2) including the energy equation (3) using a finite-volume-solver.

$$\frac{\partial \rho}{\partial t} = -\nabla(\rho \mathbf{u}) \tag{1}$$

$$\frac{\partial \rho \mathbf{u}}{\partial t} = -\nabla(\rho \mathbf{u}\mathbf{u}) - \nabla \boldsymbol{\tau} - \nabla p + \rho g \tag{2}$$

$$\frac{\partial}{\partial t}\left(\frac{1}{2}\rho \mathbf{u}^2 + \rho \mathbf{u}\right) = -\nabla \cdot \left(\frac{1}{2}\rho \mathbf{u}^2 + \rho \mathbf{u}\right)\mathbf{u} - \nabla \cdot \dot{\mathbf{q}} - (\nabla \cdot p\mathbf{u}) - (\nabla \cdot [\boldsymbol{\tau} \cdot \mathbf{u}]) + \rho(\mathbf{u} \cdot g) \tag{3}$$

Since the N-S equations are solved including the viscous term $\nabla \boldsymbol{\tau}$, dissipative properties of the surrounding fluid are taken into account and thus, acoustic streaming effects are considered. A measure whether the fluid may be treated as inviscid is given based on the ratio of the size of an obstacle $R$ and the penetration depth of the viscous wave (acoustic boundary layer) $\delta = (2\nu/\omega)^{1/2}$, where $\nu$ is the kinematic viscosity and $\omega$ the angular frequency. If $\delta << R$ the streaming is negligible and the mean force is equal to the acoustic radiation force. However, if $\delta \leq R$ the streaming effects become increasingly important until they are the dominating mechanism for $\delta >> R$ [14].

When assuming an inviscid host fluid, the time dependent acoustic drag force $F_i$ on an obstacle can be obtained by integration of the pressure field on the surface $S$ of the body [16]:

$$F_i = -\oiint_S p_s \mathbf{n_i} dS \ . \tag{4}$$

The acoustic radiation force $\overline{F_i}$ results from the time average of eq. 4 within one period $T$ of the acoustic wave [16]:

$$\overline{F_i} = \frac{1}{T}\int_T F_i dt = -\oiint_S \overline{p_s}\mathbf{n_i} dS \ . \tag{5}$$

The analytic equation for the calculation of the radiation force proposed by King [6] may be given by

$$\overline{F_i} = \frac{\pi R^2}{\rho_f c_f^2} p_{max}^2 \sin(2kx) f_K, \tag{6}$$

with $p_{max}$ being the amplitude, $\rho_f$ the density, $c_f$ the speed of sound an $k$ the wave number of the acoustic field. The parameter $f_K$ is the relative density factor. It was suggested by King to be

$$f_K = \frac{1 + \frac{2}{3}(1 - \rho_f/\rho_p)}{2 + \rho_f/\rho_p} \ . \tag{7}$$

To obtain an approximation of the radiation force exposed to relatively long ultrasonic waves ($kR << 1$), the factor was modified by Leung, Jacobi and Wang [17] as $f_{LJW}$ which is expressed by:

$$f_{LJW} = \frac{5}{8kR}\left[\frac{\sin(2kR)}{2kR} - \cos(2kR)\right]. \tag{8}$$

A further suggestion to calculate $\overline{F_i}$ was given by Gor'kov [15]:

$$\overline{F_i} = 4\pi \overline{E} k R^3 \sin(2kx)\left[\frac{\rho_p + \frac{2}{3}(\rho_p - \rho_f)}{2\rho_p + \rho_f} - \frac{1}{3}\frac{c_f^2 \rho_f}{c_p^2 \rho_p}\right], \tag{9}$$

where $\overline{E}$ is the time averaged acoustic energy density of the sound field, $\rho_p$ the density of the solid body, and $c_p$ the speed of sound in it.

## 3. Computational Method

An open source computational fluid dynamics (CFD) code is used to solve the system of partial equations. In order to provide a standing wave, the periodic normal velocity at the inlet is set to $u = u_0 \sin(\omega t)$, with $u_0$ being the velocity amplitude of the incident wave, while a reflecting wall is imposed at the opposite boundary (Fig. 2). The outer boundary is defined as non-reflecting boundary to

prevent waves scattered at the bodies or inlet and wall boundaries to be reflected at the outlet. The method used to achieve non-reflective behavior is the approach established by Thompson [18] and Poinsot and
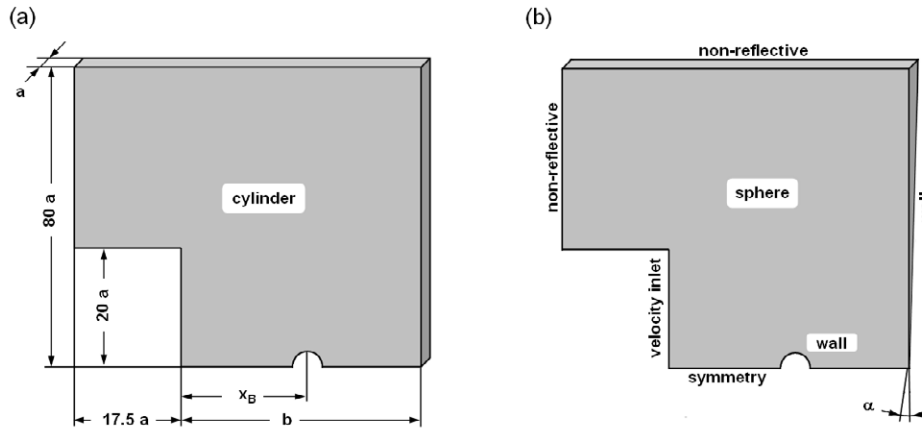


Fig. 2. Computational domain of cylinder (a) and sphere (b)

Lele [19] for subsonic non-reflective outflow. Here, each point of the boundary is represented by local one-dimensional inviscid relations (LODI Relations), neglecting transverse and viscous terms and, in addition, a physical boundary is applied to include some information about the constant pressure at infinity $p_\infty$. Thus, the outlet boundary of the domain is mathematically moved to infinity. Furthermore, symmetry and periodic boundaries are applied and a block structured mesh with grid refinement around the particle is used to reduce the computational effort.

Based on the Nyquist criteria and the Courant-Friedrich-Levy (CFL) criterion, the time step of the transient simulations was set to $\Delta t = 2 \cdot 10^{-7}$ s. The sound wave is defined by a frequency of 20 kHz for all the numerical calculations described in this paper and thus, each period of the wave is discretized by 250 time steps. The amplitude of the incident wave $u_0$ is varied between 2.51 m/s and 10.05 m/s, in order to realize elongations in the range given in Table 1. The surrounding gas is air at ambient conditions.

Table 1. Incident velocity and pressure amplitudes for given elongations Y

| Elongation $Y$ / μm | 20 | 30 | 40 | 50 | 60 | 70 | 80 |
|---|---|---|---|---|---|---|---|
| Incident velocity amplitude $u_0$ / m/s | 2.51 | 3.77 | 5.02 | 6.28 | 7.54 | 8.79 | 10.05 |
| Incident pressure amplitude $p_0$ / kPa | 1.06 | 1.59 | 2.11 | 2.64 | 3.17 | 3.70 | 4.23 |

It is here distinguished between cylindrical and spherical particle geometry. In Figure 2 the computational domains for cylinder (a) and sphere (b) are given, where the radius for both cylinder and sphere is set to $R = 0.5$ mm while the dimension of the domains is given by $a = 1$ mm, $b = 25.75$ mm and $\alpha = 5$ °. The height of the cylinder is 1 mm. To achieve a resonant standing wave the distance between acoustic source and reflecting surface $b$ has to satisfy the correlation $b = n(\lambda/2)$, with the wavelength of the incident sound wave $\lambda$ and the number of pressure nodes in the standing wave $n$. The position of the different geometries along the axis of propagation of the wave $x_B$ is varied during the examination to

provide information about the correlation of this position and the resulting forces on the considered geometries.
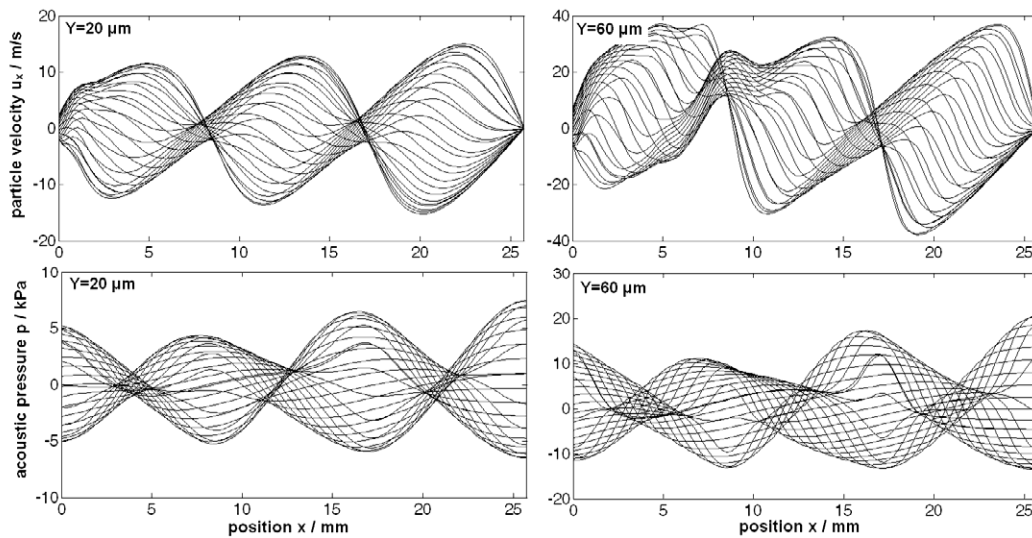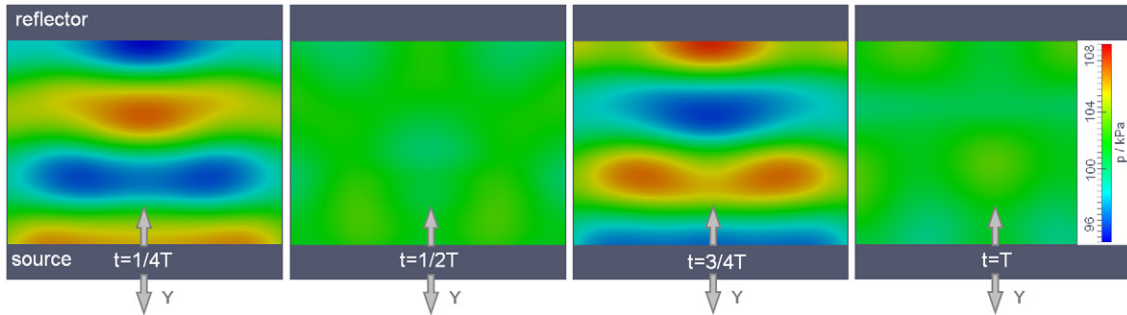




Fig. 3. Pressure field of a resonant standing wave, $Y = 20$ µm

Fig. 4. Particle velocity and acoustic pressure distribution for $Y = 20$ µm and $Y = 60$ µm along the centerline (x-axis) for equidistant time steps, $\Delta t = 2 \cdot 10^{-6}$ s within one period $T$

## 4. Numerical results

### 4.1. Resonant standing wave characterization

In order to obtain accurate characterization of the emerging forces on the considered geometries, it is crucial to obtain a precise representation of the actual sound field by computation. The pressure field of an undisturbed resonant standing wave with $Y = 20$ µm is given in Figure 3 for four certain time steps

t = 1/4 *T*; 1/2 *T*; 3/4 *T*; *T*. The comparison between these for time steps confirms the characteristic of the standing wave field. The pressure nodes and anti-nodes can easily be observed for 1/4 *T* and 3/4 *T* while no considerable pressure fluctuations can be seen for the time steps of 1/2 *T* and *T*.

Figure 4 shows the particle velocity $u_x$ and acoustic pressure distribution $p$ along the symmetry axis (x-axis) of the domain for equidistant time steps of $\Delta t = 2 \cdot 10^{-6}$ s for one period *T* and elongations $Y = 20$ µm and $Y = 60$ µm. In agreement with the theory, a phase shift of 1/4 $\lambda$ for the curves of velocity and pressure
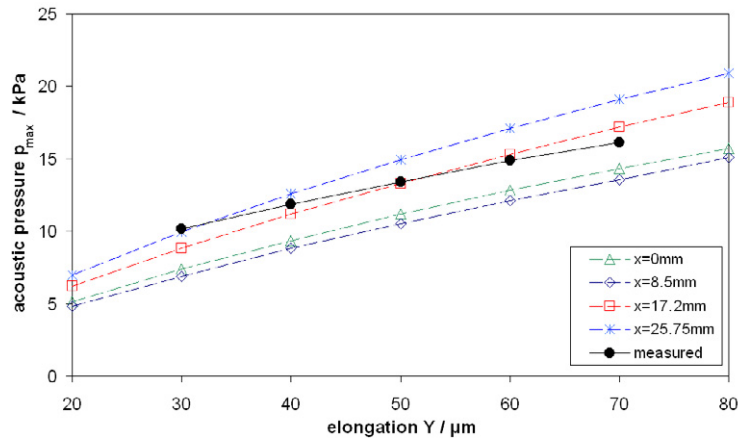


Fig. 5. Pressure field of a resonant standing wave, $Y = 20$ µm

can be observed. Furthermore, the maximum and minimum anti-nodes of velocity and pressure curves are staggered against each other so that the curves lean laterally. This effect is due to non-linear phenomena and gets more distinct for higher incident velocities. When considering the near-field of the sound source, one can see a growing disturbance of the standing wave with increasing incident velocities in this region. Since the langevin radiation [16] is considered, with taking the surrounding undisturbed atmosphere into account and the fluid is treated viscid, acoustic streaming occurs in the near-field depending on the incident velocity and hence, on the amount of energy being introduced to the host fluid.

In Figure 5 the effect of variation of the elongation on the resulting pressure amplitudes $p_{max}$ at different positions in the resonant field is given. The pressure is shown at the surface of sound source (x = 0 mm) and reflector (x = 25.75 mm) and for the pressure anti-nodes at x = 8.5 mm and x = 17.2 mm (Fig. 1). It can be noted that the pressure increases significantly with about the same gradient for all positions. However, the level is different. While the highest values are found at the reflector surface the maximum at x = 8.5 mm shows the lowest values.

A validation of the simulated wave field has been done by means of a piezo-electric measurement of the acoustic pressure inside an acoustic levitation setup. The sensor was positioned at x = 17.2 mm. Comparing the curve of the measurement with the results of the simulation at the same position (Fig. 5), one can find a difference of less than 15 % for all compared elongations.

## 4.2. Time dependent force

In order to characterize the local effect on the resulting forces, the position of the considered particles in the standing wave field $x_B$ was varied between the two pressure nodes at $x_B = 12.9$ mm and $x_B = 21.5$ mm including the anti-node at $x_B = 17.2$ mm (Fig. 1). The time dependent drag force $F_x$ exerted on cylinder and sphere for different positions in the sound field is shown in Figure 6 for the two amplitudes of $Y = 20$ µm and $Y = 60$ µm. The time $t^*$ is a non-dimensional time defined by $t^* = t/T$. All presented curves show alternating behavior with the same frequency as the applied sound field. However, there are notable differences in the amplitudes of the force $F_x$ depending on the particle position $x_B$. While the amplitudes reach a maximum value when the obstacles are located at the pressure nodes, they diminish when $x_B$ gets moved towards the pressure anti-node where the amplitudes reach a
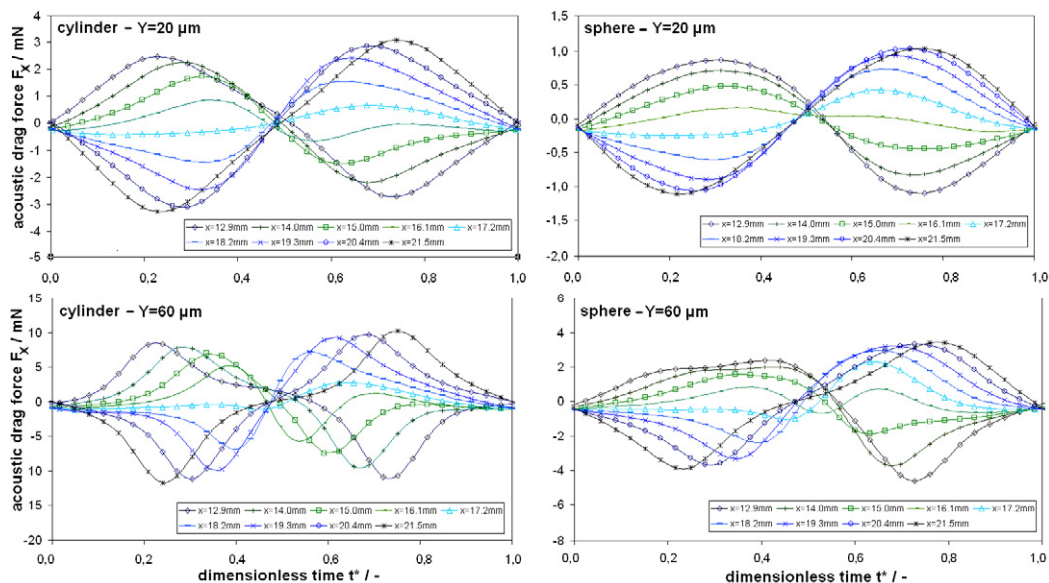


Fig. 6. Time dependent force $F_x$ on cylinder and sphere for two amplitudes at different positions $x = 12.9 \ldots 21.5$ mm

minimum value (they do not reach a value of zero due to the spatial dimension of the bodies). Moreover, the direction of $F_x$ changes when the position moves past an anti-node.

Considering the force distribution for elongations of 20 µm and 60 µm, the influence of non-linear effects can be observed as the shape of the curves changes from a wider to a narrower shape. When comparing the influence of the geometry of the particles, it can be seen that the forces exerted on the cylindrical body are significantly higher than on the spherical one. For $Y = 20$ µm force values on the cylindrical particle are in average about 2.8 times higher than the values on the spherical. In case of an elongation of 60 µm, the factor is approximately 3.3 so that it may be guessed that the difference in the acoustic force between cylinder an sphere grows with increasing elongations.

### 4.3. Time averaged radiation force

In order to attain the acoustic radiation force $\overline{F_x}$ the force distribution curves from Fig. 6 are time averaged using eq. (5). The resulting forces are plotted along the x-axis (Fig. 7a) and correlated to the analytic equations (6)-(9). For the region between pressure node at $x_B = 12.9$ mm and anti-node at $x_B = 17.2$ mm the acoustic forces are oriented towards the inlet surface, while the orientation changes towards the reflector when entering the region above $x_B = 17.2$ mm. As a result, the amplitude has a local maximum between node and anti-node and hence, oscillates with a frequency of twice the applied frequency of the resonant wave. The simulated acoustic forces on the sphere show best agreement for $Y = 20$ µm with the analytic equation proposed by King and Leung et al. especially for the region facing the reflector. In the near- source region the simulated values start to differ from the analytic solution. This behaviour can be seen in all simulated curves and it occurs due to the acoustic streaming which happens mainly in the near-field of the sound source as it can be observed in Figure 4. The cylindrical particle shows larger values than the spherical as it could be assumed based on these observations in Figure 6. For
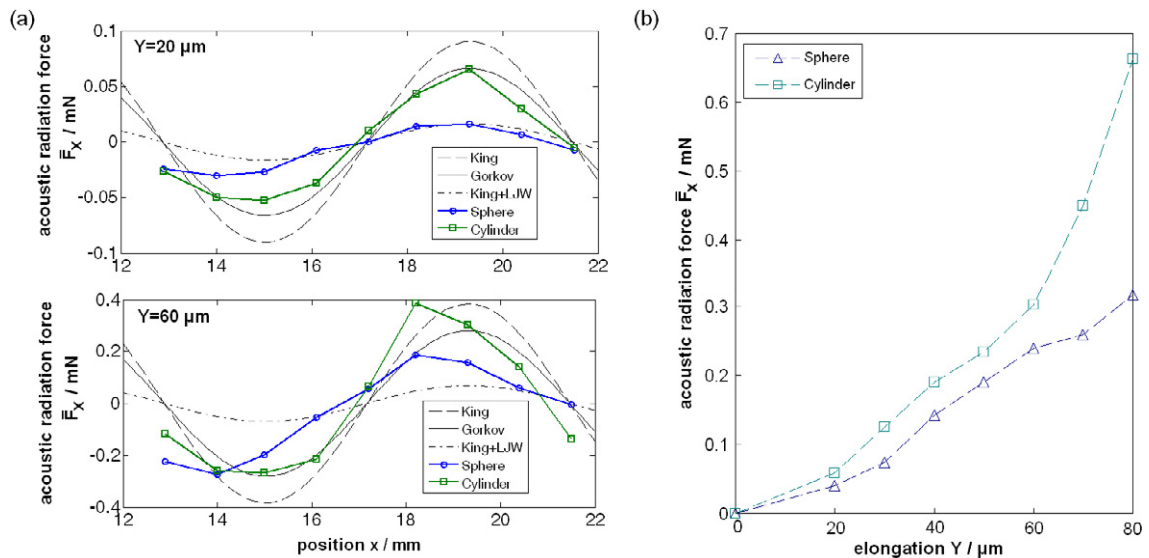


Fig. 7. Simulated and analytic time averaged radiation force on spherical and cylindrical particle depending on different positions for $Y = 20$ µm and $Y = 60$ µm (a) and acoustic radiation fore on spherical an cylindrical particle depending on the elongation (b)

the chosen parameters, the curve agrees quite well with the equation of Gor'kov.

When the elongation is increased to a value of 60 µm, the analytic equation of King and Leung et al. diverges from the simulation of the sphere. A similar trend can be seen for the cylindrical particle and the equation of Gor'kov. As described earlier, the analytic equations are valid for the assumption of inviscous fluids while the simulations include the viscous terms of the N-S equations. The acoustic boundary layer for the chosen conditions is $\delta = (2\nu/\omega)^{1/2} = 15.3$ µm and therewith one order of magnitude less than the obstacle radius. Thus, the fluid may be treated as inviscous [14]. However, the calculations show non-linear behavior depending on the elongation (Figure 4).

$$\overline{F_x}$$

In Figure 7b the amplitude of the acoustic radiation force    on cylinder and sphere is shown for increasing elongations at $x_B = 19.3$ µm. Both curves show an increasing radiation force for increased elongations with higher values for the cylinder. In comparison to the curve of the sphere, the rise in the force values of the cylinder curve is notably stronger for amplitudes above 60 µm.

### 4.4. Time dependent force on agglomerated particles

A comparison of the acoustic force $F_x$ on a spherical particle and a model agglomerate for an elongation of $Y = 20$ µm at $x_B = 19.3$ mm is given in Figure 8. The model agglomerate consists of thirteen primary particles with a size of $d_{prim} = 80$ µm. The enveloping sphere around the agglomerate has a diameter $D_{Ag}$ of 250 µm which is equal to the diameter $D$ of the spherical particle. In contrast to the previous simulations, no symmetry simplifications were set due to the asymmetric agglomerate geometry. In order to obtain a non-dimensional correlation, the forces are divided by the amplitude $F_{x,max}$ of the calculated agglomerate curve and related to the dimensionless time $t^*$ (Figure 8a). The curves show a sinusoidal behavior with no obvious influence of non-linear terms. A difference of about 100 % can be observed for the values of the spherical particle in comparison to the model agglomerate.
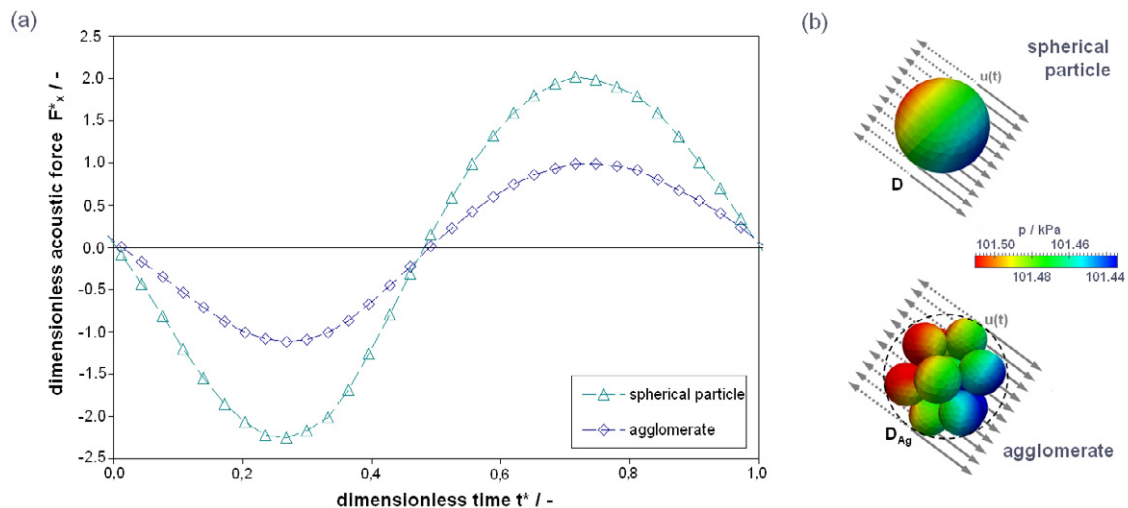


Fig. 8. Acoustic force $F^*_x$ on spherical particle and agglomerate for $Y = 20$ µm (a) and pressure distribution on particle and agglomerate surface at $t^* > 0.8$ (b)

In Figure 8b the pressure distribution on the surface of the different geometries is illustrated exemplarily for a time $t^*$ between 0 and 0.25 and 0.75 and 1 respectively. One can see a negative pressure gradient in the direction of the instantaneous flow direction (solid arrows), which leads to inhomogeneous stress conditions at the surface of the bodies. Looking at the agglomerate it is obvious, that this fact causes different stress conditions at the single primary particles and hence effects the particle-particle contact of the structure.

## 5. Conclusion

A comparison between the effect of a resonant standing wave on a cylindrical and spherical particle as well as on an agglomerate structure has been done by means of CFD. The simulated sound field could be validated with measured data and the time dependent and time averaged radiation forces were deviated for the cylindrical and spherical particles and verified by analytical equations. It could be shown that the amplitude of the incident velocity and thus the amount of energy being applied can have an effect on whether the assumption of an inviscid host fluid is valid or not. Furthermore, higher forces on cylindrical particles compared to spherical ones could be observed based on the calculated values. This trend gets further enhanced by increasing elongations.

**Nomenclature**

| | |
|---|---|
| $c$ | speed of sound in m/s |
| $\overline{E}$ | time averaged acoustic energy density in J/m³ |
| $F_i$ | time dependent acoustic drag force in N |
| $\overline{F_i}$ | acoustic radiation force in N |
| $f$ | frequency in 1/s |
| $k$ | wave number in 1/m |
| $n$ | number of pressure nodes |
| $p$ | pressure in Pa |
| $R$ | radius in m |
| $S$ | surface area in m² |
| $T$ | period in s |
| $u$ | velocity in m/s |
| $x_B$ | position of particle/agglomerate in m |
| $Y$ | elongation in m |

*Greek letters*

| | |
|---|---|
| $\delta$ | acoustic boundary layer thickness in m |
| $\lambda$ | wavelength in m |
| $\nu$ | kinematic viscosity in m²/s |
| $\rho$ | density in kg/m³ |
| $\tau$ | shear stress in Pa |

| | |
|---|---|
| $\omega$ | angular frequency in 1/s |

*Subscripts*

| | |
|---|---|
| 0 | value of the incident wave |
| f | fluid |
| max | amplitude value |
| p | particle |
| s | surface |

## Acknowledgements

## References

[1] Yarin AL, Pfaffenlehner M, Tropea C. On the acoustic levitation of droplets. *J Fluid Mech* 1998;**356**:65-91.

[2] Fritsching U, Bauckhage K. Ultrasonic field characteristics in resonant standing waves. *Ultrasonics* 1997;**35**:151-156.

[3] Fritsching U, Bauckhage K. The interaction of drops and particles with ultrasonic standing wave fields. In: Brebbia CA, Kenny J, Ciskowski RD, editors. *Computational Acoustics and its Environmental Applications*, Southampton: Computational Mechanics Publications; 1997, p. 150-168.

[4] Gröschl M. Ultrasonic separation of suspended particles – Part I: Fundamentals. *Acustica* 1998;**84**:432-447.

[5] Laurell T, Petersson F, Nilsson A. Chip integrated strategies for acoustic separation and manipulation of cells and particles. *Chem Soc Rev* 2007;**36**:492–506.

[6] King LV. On the acoustic radiation pressure on spheres. *Proc. R. Soc A* 1934;**147**:212-240.

[7] King LV. On the acoustic radiation pressure on circular discs: Inertia and diffraction corrections. *Proc R. Soc A* 1935;**153**:1-16.

[8] Awatani J. Study on acoustic pressure (VI), radiation pressure on a cylinder. *Memoirs of the Institute of Scientific and Industrial Research, Osaka University* 1955;**12**:95-102.

[9] Yosioka K, Kawasima Y. Acoustic radiation pressure on compressible sphere. *Acustica* 1955;**5**:167-173.

[10] Hasegawa T, Yosioka K. Acoustic radiation force on a solid elastic sphere. *J Acoust Soc Am* 1969;**63**:1139-1143.

[11] Hasegawa T, Saka K, Inoue N, Matsuzawa K. Acoustic radiation force experienced by a solid cylinder in a plane progressive sound field. *J Acoust Soc Am* 1988;**83**:1770-1775.

[12] Westervelt PJ. The theory of steady forces caused by sound waves. *J Acoust Soc Am* 1951;**23**:312–5.

[13] Westervelt PJ. Acoustic radiation pressure. *J Acoust Soc Am* 1957;**29**:26-29.

[14] Danilov SD, Mironov MA. Mean force on a small sphere in a sound field in a viscous fluid. *J Acoust Soc Am* 2000;**107**:143-153.

[15] Gor'kov LP. On the forces acting on a small particle in an acoustical field in an ideal fluid. *Sov Phy Dokl.* 1962;**6**:773-775.

[16] Sutilov VA. *Physik des Ultraschalls*. 1st ed. Wien, New York: Springer; 1984.

[17] Leung E, Jacobi N, Wang T. Acoustic radiation force on a rigid sphere in a resonance chamber. *J Acoust Soc Am* 1981;**70**:1962-1967.

[18] Thompson KW. Time dependent boundary conditions for hyperbolic systems. *J Comput Phys* 1987;**68**:1-24.

[19] Poinsot T, Lele S. Boundary conditions for direct simulations of compressible viscous flows. *J Comput Phys* 1992;**101**:104-129.